The Astrophysical Journal, 818:68 (14pp), 2016 February 10
doi:10.3847/0004-637X/818/1/68

MEASUREMENTS OF COSMIC-RAY HYDROGEN AND HELIUM ISOTOPES WITH THE PAMELA EXPERIMENT

O. Adriani[1,2], G. C. Barbarino[3,4], G. A. Bazilevskaya[5], R. Bellotti[6,7], M. Boezio[8], E. A. Bogomolov[9], M. Bongi[1,2], V. Bonvicini[8], S. Bottai[2], A. Bruno[6,7], F. Cafagna[7], D. Campana[4], P. Carlson[10], M. Casolino[11], G. Castellini[12], C. De Donato[13], C. De Santis[11], N. De Simone[13], V. Di Felice[13], V. Formato[8,20], A. M. Galper[14], A. V. Karelin[14], S. V. Koldashov[14], S. Koldobskiy[14], S. Y. Krutkov[9], A. N. Kvashnin[5], A. Leonov[14], V. Malakhov[14], L. Marcelli[11], M. Martucci[11,15], A. G. Mayorov[14], W. Menn[16], M Mergè[13,11], V. V. Mikhailov[14], E. Mocchiutti[8], A. Monaco[6,7], N. Mori[2], R. Munini[8,17], G. Osteria[4], F. Palma[13,11], B. Panico[4], P. Papini[2], M. Pearce[10], P. Picozza[13,11], M. Ricci[15], S. B. Ricciarini[12], R. Sarkar[18,21], V. Scotti[3,4], M. Simon[16], R. Sparvoli[13,11], P. Spillantini[1,2], Y. I. Stozhkov[5], A. Vacchi[8,19], E. Vannuccini[2], G. Vasilyev[9], S. A. Voronov[14], Y. T. Yurkin[14], G. Zampa[8], and N. Zampa[8]

[1] University of Florence, Department of Physics, I-50019 Sesto Fiorentino, Florence, Italy
[2] INFN, Sezione di Florence, I-50019 Sesto Fiorentino, Florence, Italy
[3] University of Naples "Federico II," Department of Physics, I-80126 Naples, Italy
[4] INFN, Sezione di Naples, I-80126 Naples, Italy
[5] Lebedev Physical Institute, RU-119991, Moscow, Russia
[6] University of Bari, Department of Physics, I-70126 Bari, Italy
[7] INFN, Sezione di Bari, I-70126 Bari, Italy
[8] INFN, Sezione di Trieste, I-34149 Trieste, Italy
[9] Ioffe Physical Technical Institute, RU-194021 St. Petersburg, Russia
[10] KTH, Department of Physics, and the Oskar Klein Centre for Cosmoparticle Physics, AlbaNova University Centre, SE-10691 Stockholm, Sweden
[11] University of Rome "Tor Vergata," Department of Physics, I-00133 Rome, Italy
[12] IFAC, I-50019 Sesto Fiorentino, Florence, Italy
[13] INFN, Sezione di Rome "Tor Vergata," I-00133 Rome, Italy
[14] National Research Nuclear University MEPhi, RU-115409 Moscow
[15] INFN, Laboratori Nazionali di Frascati, Via Enrico Fermi 40, I-00044 Frascati, Italy
[16] Universität Siegen, Department of Physics, D-57068 Siegen, Germany
[17] University of Trieste, Department of Physics, I-34147 Trieste, Italy
[18] Indian Centre for Space Physics, 43 Chalantika, Garia Station Road, Kolkata 700084, West Bengal, India
[19] University of Udine, Department of Mathematics and Informatics, I-33100 Udine, Italy

Received 2015 November 13; accepted 2015 December 17; published 2016 February 9

ABSTRACT

The cosmic-ray hydrogen and helium (^{1}H, ^{2}H, ^{3}He, ^{4}He) isotopic composition has been measured with the satellite-borne experiment PAMELA, which was launched into low-Earth orbit on board the *Resurs-DK1* satellite on 2006 June 15. The rare isotopes ^{2}H and ^{3}He in cosmic rays are believed to originate mainly from the interaction of high-energy protons and helium with the galactic interstellar medium. The isotopic composition was measured between 100 and 1100 MeV/n for hydrogen and between 100 and 1400 MeV/n for helium isotopes using two different detector systems over the 23rd solar minimum from 2006 July to 2007 December.

Key words: astroparticle physics – cosmic rays

1. INTRODUCTION

The rare isotopes ^{2}H and ^{3}He in cosmic rays are generally believed to be of secondary origin, resulting mainly from the nuclear interactions of primary cosmic-ray protons and ^{4}He with the interstellar medium. The spectral shape and composition of the secondary isotopes are therefore completely determined by the source spectrum of the parent elements and by the propagation process. Measurements of the secondary isotope spectra are then a powerful tool to constrain the parameters of the galactic propagation models (Heinbach & Simon 1995; Strong et al. 2007; Coste et al. 2012; Tomassetti 2012).

The first measurements of hydrogen and helium isotopes became available in the 1970s (Garcia-Munoz et al. 1975a, 1975b; Mewaldt et al. 1976; Leech & O'Gallagher 1978), but were limited to energies below 100 MeV/n. The identification, especially at energies greater than 100 MeV/n, is quite difficult, due to the high experimental mass resolution required to distinguish the secondary nuclei from the abundant background of primaries. In the 1980s and 1990s there were several measurements of stratospheric balloon experiments using superconducting magnetic spectrometers (Webber et al. 1991; Beatty et al. 1993; Reimer et al. 1998; Wefel et al. 1995; Wang et al. 2002) and also a measurement from AMS-01 (Aguilar et al. 2011) in space. While the mass resolution of the balloon experiments was usually quite good, the residual atmosphere above the instruments caused a nonnegligible background of secondary particles. The atmospheric background estimation is subject to large uncertainties (e.g., the limited knowledge of isotope production cross sections).

The results presented in this paper are based on data gathered between 2006 July and 2007 December with the PAMELA satellite experiment. PAMELA has been put in a polar elliptical orbit at an altitude between ~350 and ~600 km with an inclination of 70° as part of the Russian *Resurs-DK1* spacecraft. Because of the low-earth orbit, the measurements are performed in an environment free from the background induced by interactions of cosmic rays within the atmosphere. The month of 2006 December was discarded from the data set

---

[20] Now at INFN, Sezione di Perugia, I-06123 Perugia, Italy.

[21] Previously at INFN, Sezione di Trieste, I-34149 Trieste, Italy.

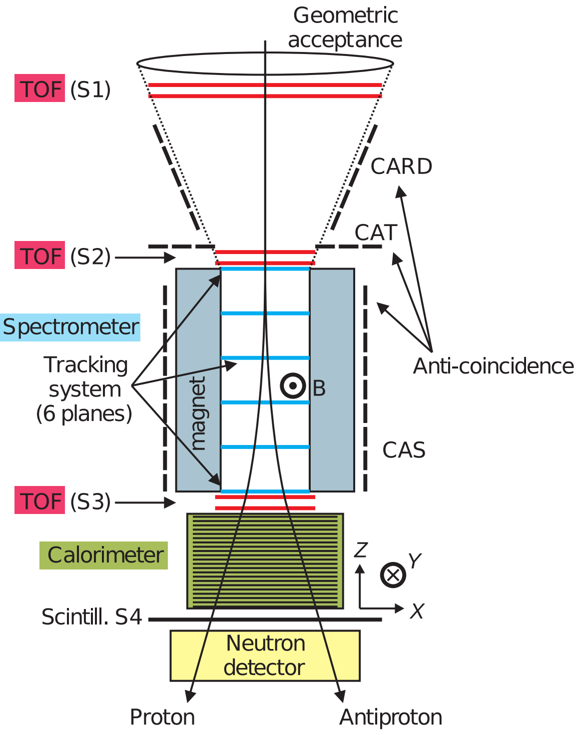

Figure 1. Scheme of the detectors composing the PAMELA satellite experiment.

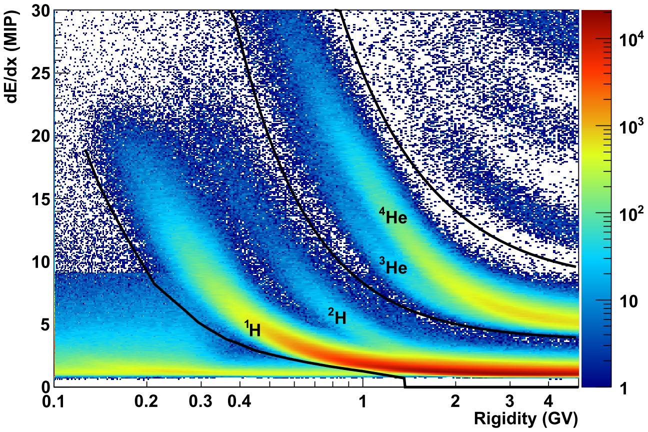

Figure 2. Ionization loss (dE/dx in MIP, energy loss of minimum ionizing particles) in the silicon detectors of the tracking system as a function of reconstructed rigidity. The black lines represent the selection for $Z = 1$ or $Z = 2$ nuclei.

to avoid possible biases from the solar particle events that took place during December 13 and 14. During a total acquisition time of 528 days, about 10^9 triggered events were recorded, and $5.8 \cdot 10^6$ hydrogen nuclei were selected in the energy interval between 100 and 1100 MeV/n, and $1.6 \cdot 10^6$ helium nuclei between 100 and 1400 MeV/n.

This is the second paper on isotopes from the PAMELA instrument. The first paper (Adriani et al. 2013b) dealt with the same isotopes ^{1}H, ^{2}H, ^{3}He, and ^{4}He but used solely the combination of velocity measurement provided by the time-of-flight system with the momentum measurement of the magnetic spectrometer. In this work, we employed a more advanced and a more comprehensive analysis. In detail, a more complete and elaborated fitting procedure was employed,

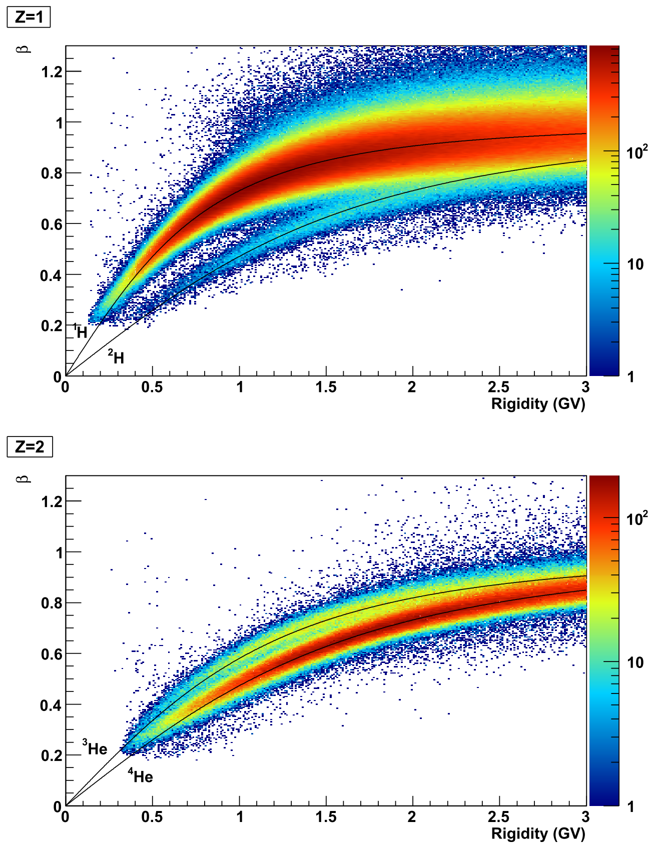

Figure 3. β versus rigidity for $Z = 1$ (top) and $Z = 2$ (bottom) particles. The black lines were calculated for each isotope using Equation (1).

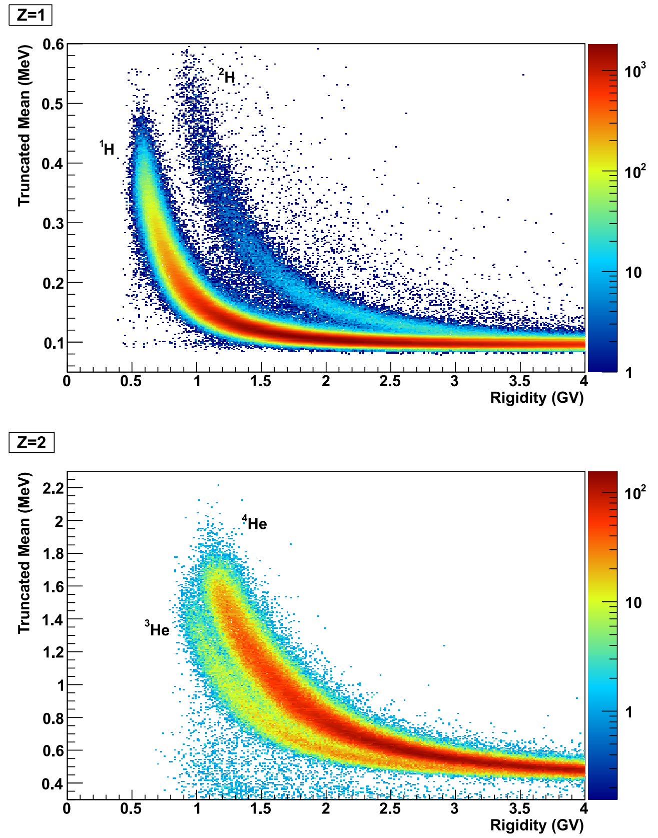

Figure 4. Mass separation for $Z = 1$ (top) and $Z = 2$ (bottom) particles using the "truncated-mean" method.

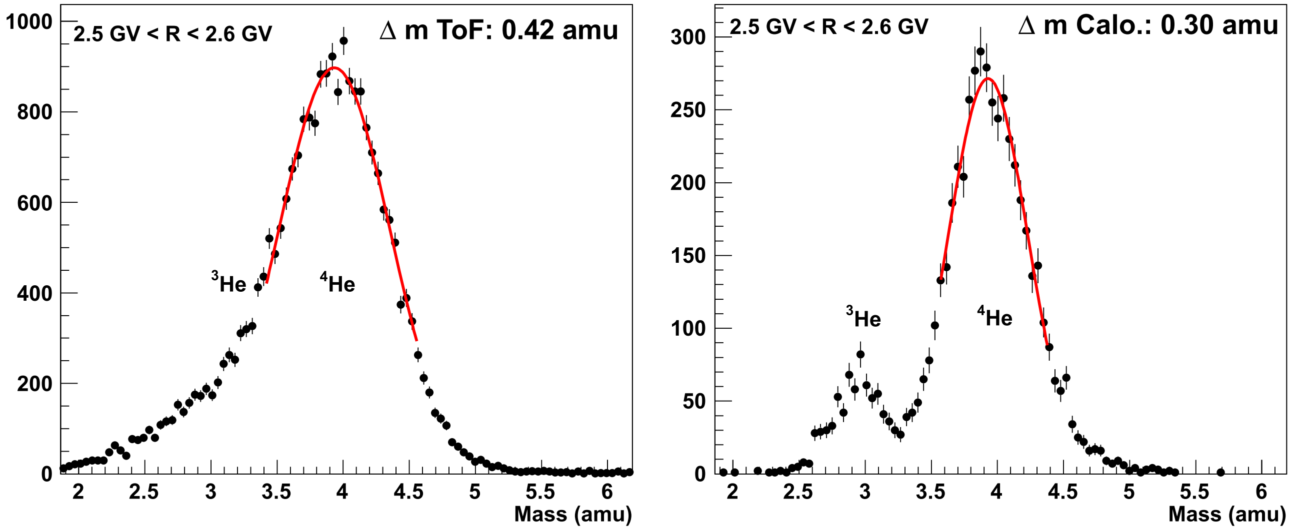

Figure 5. Example mass distributions for helium in the 2.5–2.6 GV rigidity range for ToF (left) and calorimeter (right).

combined with a more stringent selection on cuts and on efficiencies. In addition, we made use of the multiple energy loss measurements provided by the 44 planes of the imaging calorimeter. This not only allowed a cross-check between the two techniques of isotopic separation within the PAMELA instrument (time-of-flight (ToF) and multiple dE/dx versus rigidity), but the multiple dE/dx technique also allowed us to extend the measurements for isotopes to higher energies: for hydrogen isotopes the highest energy bin is now at 1035 MeV/n (instead of 535 MeV/n), while for helium it is now at 1297 MeV/n (instead of 823 MeV/n). Additionally, the previous results (Adriani et al. 2013b) were revised in this improved analysis.

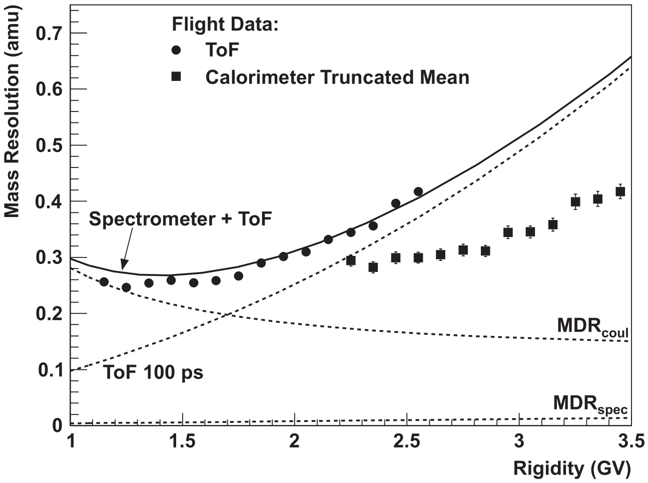

Figure 6. Measured ^{4}He mass resolution for the ToF (circles) and the calorimeter using the "truncated-mean" method (squares). If the error bars are not visible, they lie inside the data points. The dashed lines show the calculated independent contributions (rigidity ($\mathrm{MDR_{spec}}$), multiple scatter ($\mathrm{MDR_{cou}}$), and velocity via ToF (time resolution 100 ps)), and the solid lines show the overall mass resolution for this combination.

2. THE PAMELA APPARATUS

A schematic view of the PAMELA detector system (Picozza et al. 2007) is shown in Figure 1. The design was chosen to meet the main scientific goal of precisely measuring the light components of the cosmic-ray spectrum in the energy range starting from tens of megaelectronvolts up to 1 TeV (depending on particle species), with a particular focus on antimatter. Thus the design is optimized for $Z = 1$ particles and a high lepton/hadron discrimination power.

The instrument core is a permanent magnet with a silicon microstrip tracker. The design of the permanent magnet provides an almost uniform magnetic field of 0.45 T inside the magnetic cavity. Six layers of 300 μm thick double-sided microstrip silicon detectors are used to measure particle deflection with ~3 μm and ~11 μm precision (measured with beam tests and flight data) in the bending and nonbending views, respectively. Because of the small size, the amount of material inside the magnetic cavity can be kept to a minimum, only six layers of silicon without any need for a support structure. The maximum detectable rigidity (MDR) of the magnetic spectrometer is about 1 TV.

The ToF system comprises six layers of fast plastic scintillators arranged in three planes (S1, S2, and S3). Each detector layer is segmented into strips, placed in alternate layers orthogonal to each other. Using different combinations of layers, the ToF system can provide 12 measurements of the particle velocity, $\beta = v/c$, and, using a weighted-mean technique, an overall value for β is calculated from these measurements. The overall time resolution of the ToF system is about 250 ps for $Z = 1$ particles and about 100 ps for $Z = 2$ particles. This allows albedo particles crossing PAMELA from bottom to top to be discarded by requiring a positive β. The ToF scintillators can also identify the absolute particle charge up to oxygen by means of the six independent ionization measurements.

The silicon–tungsten electromagnetic sampling calorimeter comprises 44 single-sided silicon planes interleaved with 22 plates of tungsten absorbers. The calorimeter is mounted below the spectrometer, and its primary use is lepton/hadron separation (Boezio et al. 2002). Each tungsten layer has a thickness of 0.74 radiation lengths (2.6 mm), and it is sandwiched between two printed circuit boards, which house the silicon detectors as well as the front-end and digitizing electronics. Each silicon plane consists of 3 × 3, 380 μm thick, 8 × 8 cm^2 detectors, segmented into 32 strips with a pitch of 2.4 mm. The orientation of the strips for two consecutive silicon planes is shifted by 90°, thus providing two-dimensional

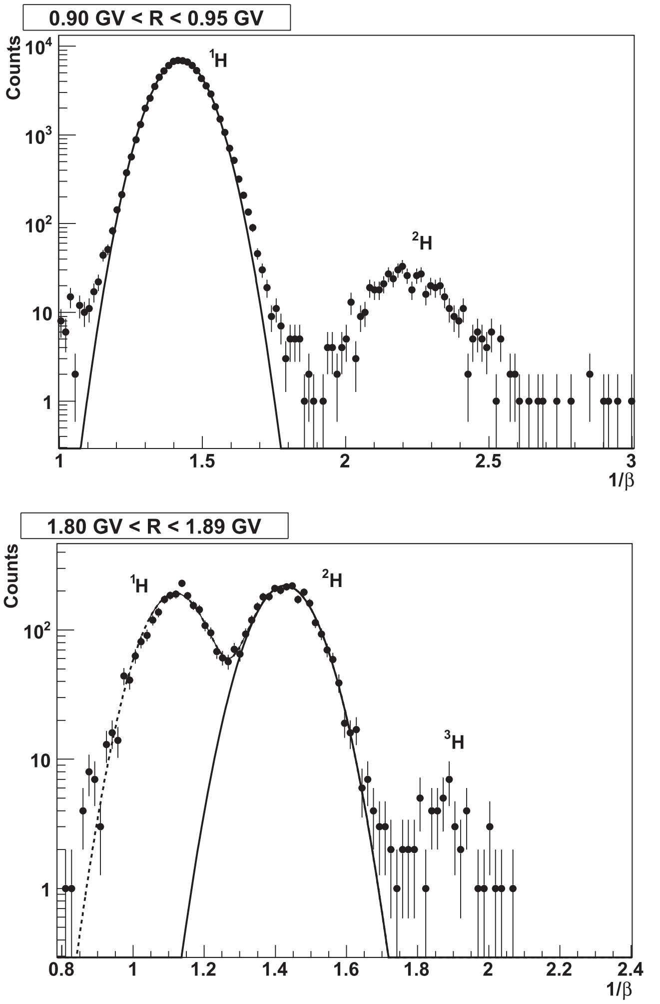

Figure 7. 1/β distributions for hydrogen in the 0.361–0.395 GeV/n kinetic energy range for ^{1}H (top) and ^{2}H (bottom). The dashed line shows the combined fit (only for ^{2}H), and the solid line shows the ^{1}H and ^{2}H individual Gaussians. Note that the ^{1}H component in the ^{2}H distribution in the bottom plot is suppressed by the additional selection cuts on the energy loss in the ToF and tracker. In the bottom figure the small fraction of ^{3}H events is visible.

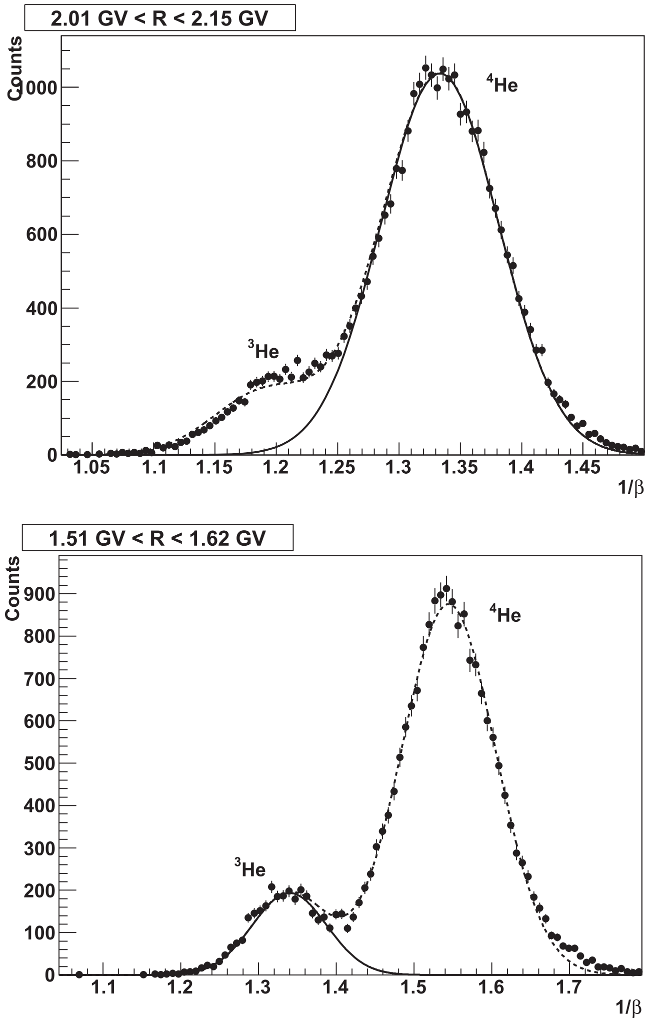

Figure 8. 1/β distributions for helium in the 0.439–0.492 GeV/n kinetic energy range for ^{4}He (top) and ^{3}He (bottom). The dashed line shows the combined fit, and the solid line shows the ^{4}He and ^{3}He individual Gaussians.

spatial information. The total depth of the calorimeter is 16.3 radiation lengths and 0.6 nuclear interaction lengths. Below the calorimeter there is a shower tail catcher scintillator (S4) and a neutron detector, which help to increase hadron/lepton separation. The tracking system and the upper ToF system are shielded by an anticoincidence system (AC) made of plastic scintillators and arranged in three sections (CARD, CAT, and CAS in Figure 1), which allows us to detect during offline data analysis the presence of secondary particles generating a false trigger or the signature of a primary particle suffering an inelastic interaction. The total weight of PAMELA is 470 kg, and the power consumption is 355 W. A more detailed description of the instrument can be found in Picozza et al. (2007).

3. DATA ANALYSIS

3.1. Event Selection

Each triggered event had to fulfill several criteria to be used for further analysis. The requirements are identical to the selection in Adriani et al. (2013b), and we refer to that paper for more details:

1. Event quality selections: We have selected events that do not produce secondary particles by requiring a single track fitted within the spectrometer fiducial acceptance and a maximum of one paddle hit in the two top scintillators of the ToF system. The analysis procedure was similar to previous work on high-energy proton and helium fluxes (Adriani et al. 2011).
2. Galactic particle selection: Galactic events were selected by imposing that the lower edge of the rigidity bin to which the event belongs exceeds the critical rigidity, ρ_c, defined as 1.3 times the cutoff rigidity ρ_{SVC} computed in the Störmer vertical approximation (Shea et al 1987) as $\rho_{\text{SVC}} = 14.9/L^2$, where L is the McIlwain L-shell parameter obtained by using the *Resurs-DK1* orbital information and the IGRF magnetic field model (MacMillan & Maus 2005).
3. Charge selection: The charge identification uses the ionization measurements provided by the silicon sensors of the magnetic spectrometer. Depending on the number

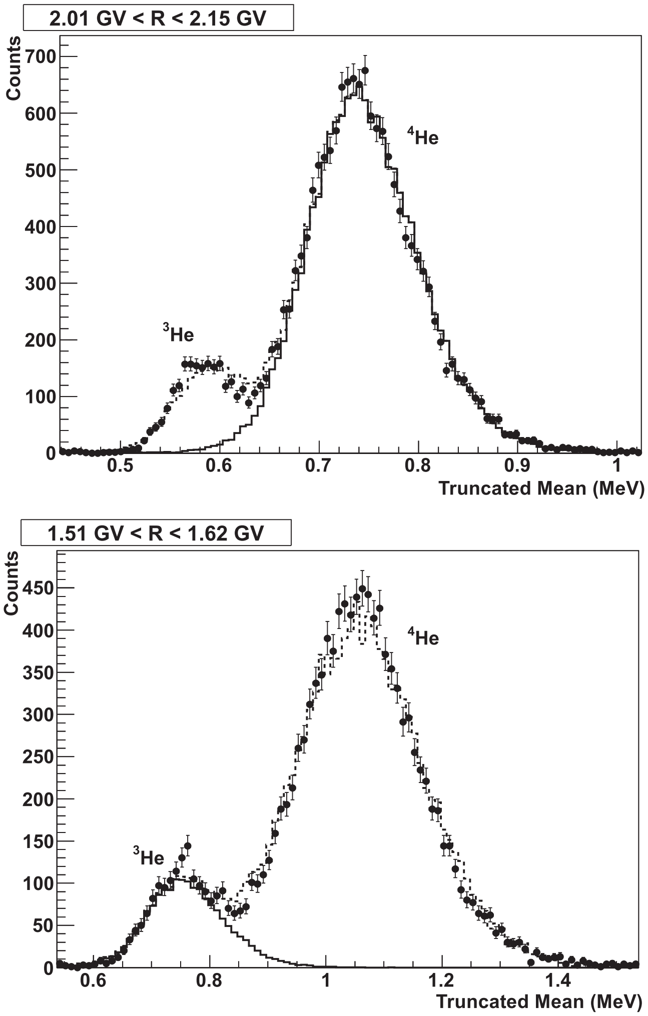

Figure 9. Example of the truncated mean distributions for helium in the 0.439–0.492 GeV/n kinetic energy range for ^{4}He (top) and ^{3}He (bottom). The dashed line shows how the combined fit using the two PDFs derived with the modified `GEANT4` simulation matches the data points (black points), and the solid line shows the estimated ^{4}He and ^{3}He individual signals.

of hit sensors, there can be up to 12 dE/dx measurements. The arithmetic mean of those measurements is shown in Figure 2 as a function of the rigidity. The actual selection of $Z = 1$ or $Z = 2$ particles is depicted by the solid lines. A similar figure has already been shown in Adriani et al. (2013b) but was kept in this paper to help the reader.

3.2. Isotope Separation in the PAMELA Instrument

In each sample of $Z = 1$ and $Z = 2$ particles, an isotopic separation at fixed rigidity is possible since the mass of each particle follows the relation

$$m = \frac{RZe}{\gamma\beta c}, \tag{1}$$

where R is the magnetic rigidity, Ze is the particle charge, and γ stands for the Lorentz factor. The particle velocity β can be provided either directly from the timing measurement of the ToF system, or indirectly from the energy loss in the calorimeter, which follows β via the Bethe-Bloch formula: $dE/dx \propto \frac{Z^2}{\beta^2}$ (neglecting logarithmic terms).

3.2.1. Isotope Separation Using ToF versus Rigidity

For the ToF analysis, we can use directly the β provided by the timing measurement. In Figure 3 we show β versus the particle rigidity for $Z = 1$ and $Z = 2$ data. The black lines in the figure represent the expectations for each isotope. A similar figure has already been shown in Adriani et al. (2013b) but was kept in this paper for an easier comparison with the alternative identification method using the calorimeter.

Since the particle mass is calculated using Equation (1), misidentified ^{4}He wrongly reconstructed as $Z = 1$ particles could result in a significant contamination to the ^{2}H sample. However, the amount of misidentified helium was found to be negligible; see Adriani et al. (2013b) for more details.

3.2.2. Isotope Separation Using Multiple dE/dx in the Calorimeter versus Rigidity

The isotopic analysis of nuclei with the calorimeter is restricted to events that do not interact inside the calorimeter. To check if an interaction occurs, we derived in each silicon layer (1) the total energy detected (q_{tot}) and (2) the energy deposited in the strip closest to the track and the neighboring strip on each side (q_{track}). In the ideal case, the fraction of $q_{\mathrm{track}}/q_{\mathrm{tot}}$ will be equal to one; a value less than one means that strips outside the track were hit. Starting from the top of the calorimeter, we calculated $\Sigma q_{\mathrm{track}}/\Sigma q_{\mathrm{tot}}$ at each layer; as long as this value was greater than 0.9, we used these layers for further analysis. A value of 0.9 was chosen since it was found to give a good compromise between high efficiency and rejection of interactions. In this way we can make use of slow particles, which stop early in the calorimeter, particles that interact somewhere, and also all clean events with the particle fully traversing the calorimeter. In the single silicon layer, the energy loss distributions show a Landau tail that degrades the resolution of the dE/dx measurement. Using a truncation method, the 50% of samples with larger pulse amplitudes were excluded before taking the mean of the dE/dx measurements, thus reducing the effect of the Landau tail. We put an energy-dependent lower limit on the number of layers after the 50% truncation, requiring at least five measurements at 1 GV, going up to 10 layers at 3 GV. With this requirement the lower energy limit of our analysis is around 200–300 MeV/n (the energy to fully penetrate the calorimeter is much higher, about 400–500 MeV/n).

In Figure 4 we show the mean dE/dx for each event versus the rigidity measured with the magnetic spectrometer for $Z = 1$ and $Z = 2$ particles. The energy loss in MeV was calculated from the measurement in MIP using a conversion factor (the most probable energy loss of a minimum ionizing particle traversing 380 μm of silicon, derived by simulation). In both plots the isotopic separation is clearly visible. It is worthwhile to mention that the selection procedure described above can be done in different ways, but we found that we achieved the best results, particularly on the corresponding efficiency (see Section 3.4), with the method described above.

The use of the calorimeter for isotope separation provides us with another advantage. Contrary to the β versus rigidity technique with the ToF, by using the multiple dE/dx versus rigidity technique, a misidentified ^{4}He wrongly reconstructed as $Z = 1$ particles would not result in a contamination to the ^{2}H sample because the dE/dx is different. This applies also for the $Z = 1$ contamination and contamination by heavier nuclei in

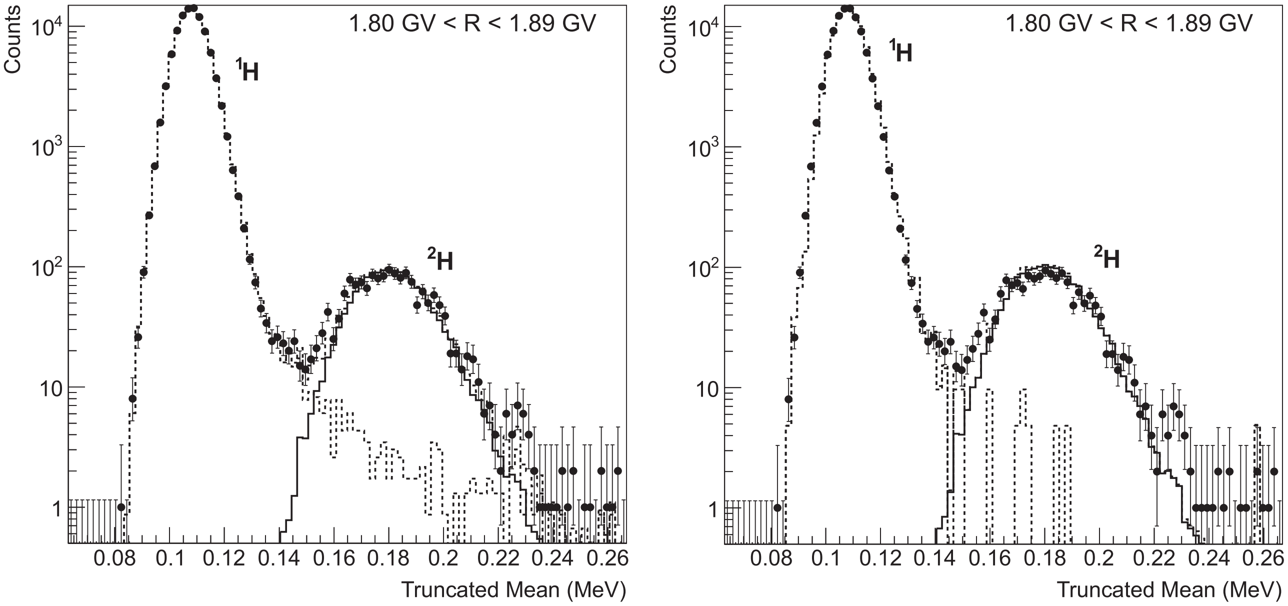

Figure 10. Example RooFit of ^{2}H. Black points: data; dashed line: ^{1}H model; solid line: ^{2}H model. The ^{2}H model is taken from the simulation for both plots, and in the left plot the ^{1}H model is derived from flight data and from simulation in the right plot.

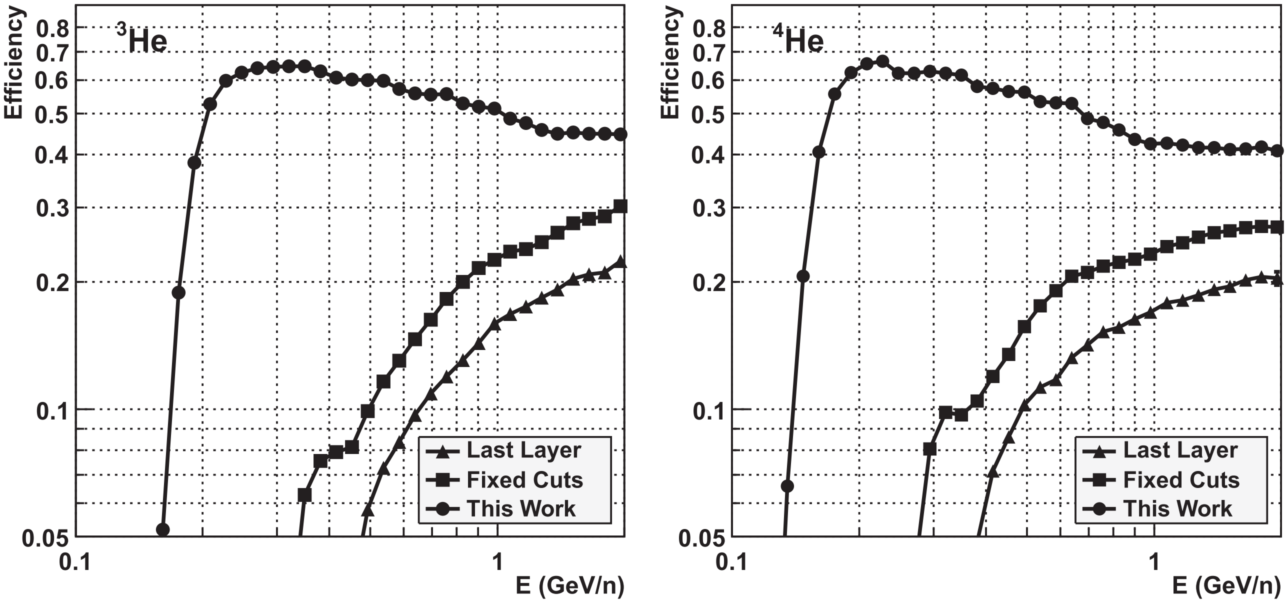

Figure 11. Calorimeter selection efficiency for helium derived with simulated data: triangles: dE/dx signal in the last layer; squares: fixed cuts (30 hit silicon strips); circles: dynamic cuts used for this work.

the $Z = 2$ sample. This allows a valuable cross-check between the results from the ToF and the calorimeter in the energy regime where the two measurements overlap.

3.2.3. Measured Mass Resolution in the PAMELA Instrument and Comparison with Expectations

Theoretically, there are three independent contributions to the mass resolution in a magnet spectrometer similar to PAMELA: the bending power of the magnetic spectrometer coupled with the intrinsic limits of spatial resolution that the tracking detectors provide, the precision of the velocity measurement (given either by timing or by measuring the energy loss), and the multiple scattering of the particle along its path in the bending area of the magnet. These three independent contributions can be expressed by the following equation:

$$dm = m\sqrt{\gamma^4\left(\frac{d\beta}{\beta}\right)^2 + \left(\frac{R}{\mathrm{MDR_{spec}}}\right)^2 + \left(\frac{R}{\mathrm{MDR_{cou}}}\right)^2}, \qquad (2)$$

where γ is the Lorentz factor, $d\beta/\beta$ is the relative error in the velocity measurement, $R/\mathrm{MDR_{spec}}$ stands for the contribution solely given by the magnetic spectrometer, and the last term stands for multiple coulomb scattering. The last two terms of

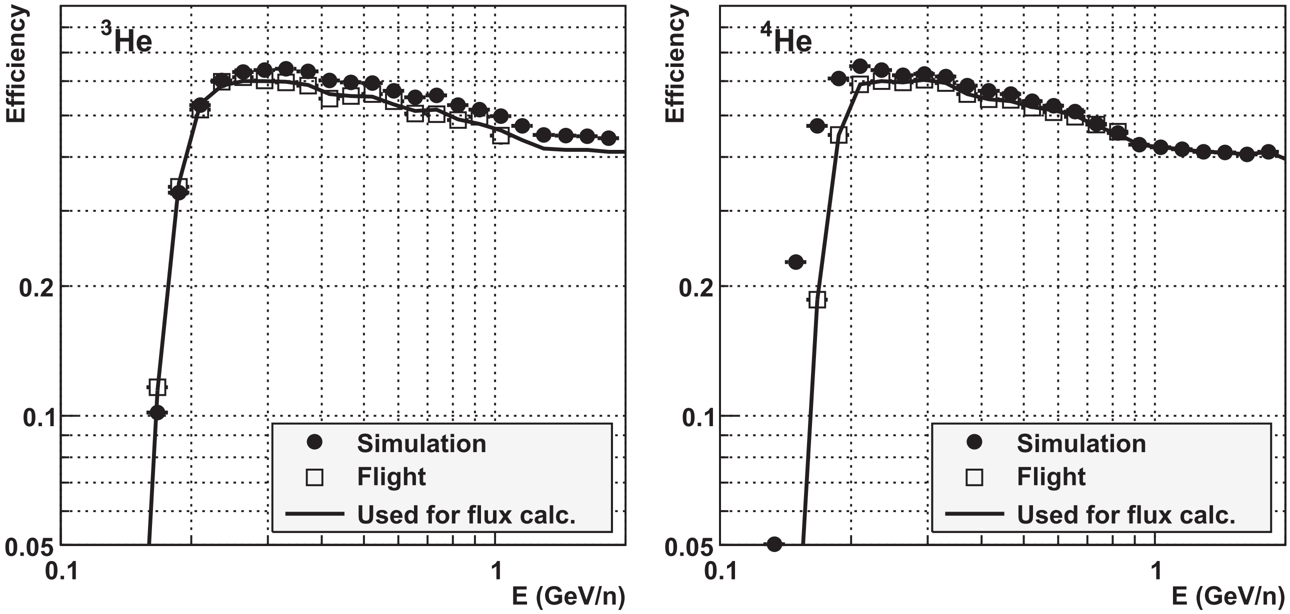

Figure 12. Comparison between the efficiency derived with simulated data (circles) and flight data (squares). The solid line shows the efficiency used for the analysis.

Equation (2) can be expressed by an overall $\mathrm{MDR_{tot}}$:

$$\left(\frac{1}{\mathrm{MDR_{tot}}}\right)^2 = \left(\frac{1}{\mathrm{MDR_{spec}}}\right)^2 + \left(\frac{1}{\mathrm{MDR_{cou}}}\right)^2. \quad (3)$$

For PAMELA the overall momentum resolution of the magnetic spectrometer (thus $\mathrm{MDR_{tot}}$) has been measured in beam tests at CERN (Picozza et al. 2007). From these measurements at high energies, where the contributions from multiple scattering are negligible, one can derive that the $\mathrm{MDR_{spec}}$ of the PAMELA spectrometer has a value of about 1 TV for $Z = 1$ particles. The contribution of $\mathrm{MDR_{spec}}$ to the overall mass resolution is therefore negligible for the particles we are analyzing (up to some gigavolts). At low rigidities, the contribution from multiple scattering is however the dominant effect. Its value is inversely proportional to the bending power of the magnet ($\int B \cdot dl$) and directly proportional to the amount of matter traversed along the bending part of the track. For an experiment using a permanent magnet in combination with silicon strip detectors, PAMELA shows a very good momentum resolution, which is due to its strong magnetic field of 0.45 T combined with a low amount of material (only the six silicon detectors, each 300 μm, giving a grammage of 0.42 g cm^{-2}) in the magnetic cavity. The overall momentum resolution was measured at CERN to have a minimum of about 3.5% at 8 GV, increasing to 5% at 1 GV (Picozza et al. 2007). Using Equation (3) one can derive the respective values for $\mathrm{MDR_{cou}}$.

By using the β-rigidity technique (see Figure 3), Equation (1) directly provides the mass of the particle, and a corresponding mass (amu) histogram for helium in the rigidity range from 2.5 to 2.6 GV is shown in Figure 5 (left). When using the multiple dE/dx versus rigidity technique (see Figure 4), a mass of either 3 or 4 amu was allocated to the corresponding peaks in the histogram. By scaling between these positions linearly, one obtains the mass distribution, which we also show for helium and for the same rigidity range of 2.5–2.6 GV in Figure 5 (right). We fitted a Gaussian to the ^{4}He peak and used the standard deviation of the Gaussian as the mass resolution, in this example 0.42 amu with the ToF, while it is 0.30 amu for the calorimeter. Thus the use of the multiple dE/dx in the calorimeter stack provided a better mass resolution than the direct measurement of β with the ToF for this rigidity interval.

We repeated this procedure for a number of rigidity intervals and derived the mass resolutions for helium obtained with the ToF and calorimeter as a function of the rigidity, which is shown in Figure 6, compared with the predictions as obtained and derived from the CERN tests. The solid black line illustrates the predicted overall mass resolution for a ^{4}He particle resulting from three contributions (shown as dotted lines): rigidity ($\mathrm{MDR_{spec}}$), multiple scatter ($\mathrm{MDR_{cou}}$), and velocity via ToF (time resolution 100 ps). As one can see, the experimental results on the mass resolution obtained from the combination of rigidity and velocity from the ToF system nicely follow the prediction. This gives us confidence that we understand our instrument. It can also be seen that the multiple dE/dx from the calorimeter provide a better mass resolution at higher energies than measuring the velocity via the ToF. This allows us to extend the PAMELA measurements on isotopes to higher energies. It can also be clearly seen that the multiple scatter sets the lower limit of the mass resolution at rigidities below roughly 2 GV no matter how high the MDR of the spectrometer is.

3.3. Raw Isotope Numbers

We had two complementary experimental methods to separate the isotopes: the combination of magnetic spectrometer either with the ToF or with the multiple dE/dx measurements within the calorimeter. In the following we will describe these procedures separately.

The isotope separation and the determination of isotope fluxes were performed identically to Adriani et al. (2013b) in intervals of kinetic energy per nucleon. Since the magnetic spectrometer measures the rigidity of particles and not the kinetic energy, this means that different rigidity intervals have

Table 1

Hydrogen Isotope Fluxes and Their Ratio Derived with the ToF; Errors Are Statistical and Systematic, Respectively

Kinetic Energy at Top of Payload (GeV n^{-1})	^{1}H Flux (GeV n^{-1} m^2 s sr)$^{-1}$	^{2}H Flux (GeV n^{-1} m^2 s sr)$^{-1}$	$^2H/^1H$
0.120–0.132	$(1.003 \pm 0.015 \pm 0.043) \cdot 10^3$	$(33.9 \pm 0.9 \pm 1.5)$	$(3.38 \pm 0.11 \pm 0.30) \cdot 10^{-2}$
0.132–0.144	$(1.062 \pm 0.014 \pm 0.044) \cdot 10^3$	$(35.5 \pm 0.9 \pm 1.5)$	$(3.34 \pm 0.09 \pm 0.28) \cdot 10^{-2}$
0.144–0.158	$(1.128 \pm 0.013 \pm 0.045) \cdot 10^3$	$(36.0 \pm 0.8 \pm 1.4)$	$(3.19 \pm 0.08 \pm 0.25) \cdot 10^{-2}$
0.158–0.173	$(1.186 \pm 0.012 \pm 0.045) \cdot 10^3$	$(36.6 \pm 0.7 \pm 1.4)$	$(3.08 \pm 0.07 \pm 0.24) \cdot 10^{-2}$
0.173–0.190	$(1.239 \pm 0.012 \pm 0.046) \cdot 10^3$	$(36.7 \pm 0.7 \pm 1.4)$	$(2.96 \pm 0.06 \pm 0.22) \cdot 10^{-2}$
0.190–0.208	$(1.296 \pm 0.011 \pm 0.047) \cdot 10^3$	$(37.7 \pm 0.7 \pm 1.4)$	$(2.91 \pm 0.06 \pm 0.21) \cdot 10^{-2}$
0.208–0.228	$(1.346 \pm 0.010 \pm 0.048) \cdot 10^3$	$(38.0 \pm 0.6 \pm 1.4)$	$(2.82 \pm 0.05 \pm 0.21) \cdot 10^{-2}$
0.228–0.250	$(1.406 \pm 0.010 \pm 0.050) \cdot 10^3$	$(37.7 \pm 0.6 \pm 1.4)$	$(2.68 \pm 0.04 \pm 0.19) \cdot 10^{-2}$
0.250–0.274	$(1.456 \pm 0.009 \pm 0.051) \cdot 10^3$	$(36.5 \pm 0.5 \pm 1.3)$	$(2.51 \pm 0.04 \pm 0.18) \cdot 10^{-2}$
0.274–0.300	$(1.487 \pm 0.009 \pm 0.052) \cdot 10^3$	$(35.7 \pm 0.5 \pm 1.3)$	$(2.40 \pm 0.03 \pm 0.17) \cdot 10^{-2}$
0.300–0.329	$(1.513 \pm 0.008 \pm 0.052) \cdot 10^3$	$(35.2 \pm 0.4 \pm 1.2)$	$(2.32 \pm 0.03 \pm 0.16) \cdot 10^{-2}$
0.329–0.361	$(1.513 \pm 0.007 \pm 0.052) \cdot 10^3$	$(34.6 \pm 0.4 \pm 1.2)$	$(2.29 \pm 0.03 \pm 0.16) \cdot 10^{-2}$
0.361–0.395	$(1.520 \pm 0.007 \pm 0.052) \cdot 10^3$	$(33.6 \pm 0.4 \pm 1.2)$	$(2.21 \pm 0.03 \pm 0.15) \cdot 10^{-2}$
0.395–0.433	$(1.499 \pm 0.006 \pm 0.051) \cdot 10^3$	$(33.4 \pm 0.4 \pm 1.2)$	$(2.23 \pm 0.03 \pm 0.16) \cdot 10^{-2}$
0.433–0.475	$(1.487 \pm 0.006 \pm 0.050) \cdot 10^3$	$(32.3 \pm 0.4 \pm 1.2)$	$(2.17 \pm 0.03 \pm 0.15) \cdot 10^{-2}$
0.475–0.520	$(1.469 \pm 0.006 \pm 0.050) \cdot 10^3$	$(31.0 \pm 0.4 \pm 1.2)$	$(2.11 \pm 0.03 \pm 0.15) \cdot 10^{-2}$
0.520–0.570	$(1.397 \pm 0.005 \pm 0.047) \cdot 10^3$	$(29.4 \pm 0.3 \pm 1.3)$	$(2.10 \pm 0.03 \pm 0.16) \cdot 10^{-2}$

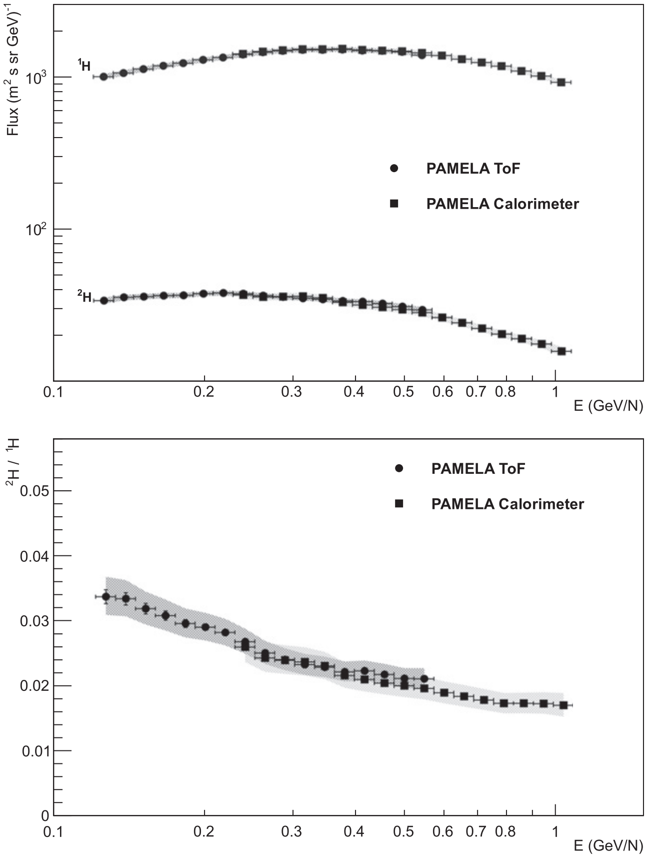

Figure 13. ^{1}H and ^{2}H absolute fluxes (top) and their ratio (bottom) derived with the ToF (circles) or the calorimeter (squares). Error bars show the statistical uncertainty, and shaded areas show the systematic uncertainty.

to be analyzed depending on the mass of the isotope under study. For example, Figure 7 shows the $1/\beta$ distributions used to select ^{1}H (top panel) and ^{2}H (bottom panel) in the kinetic energy interval 0.361–0.395 GeV/n corresponding to 0.90–0.95 GV for ^{1}H and 1.80–1.89 GV for ^{2}H.

3.3.1. Raw Isotope Numbers with the ToF

The particle counts in each rigidity range were derived in a similar manner as in Adriani et al. (2013b) by fitting Gaussians to the $1/\beta$ distributions, as shown by the solid lines in Figure 7. Instead of mass distributions (shown in Figure 5), $1/\beta$ distributions were chosen since the shape of a $1/\beta$ distribution is Gaussian, while the mass distribution is not. (Note that for the estimation of the mass resolution in Section 3.2.3 this feature could be neglected.)

The ^{1}H peak in Figure 7 (top) is well pronounced and barely affected by the shape of the neighboring ^{2}H distribution. For that reason a single Gaussian was fitted to the ^{1}H peak, as shown in Figure 7 (top). For the fitting method the ROOT analysis package (Brun & Rademakers 1997) was used. The Gaussian fit to the ^{2}H, ^{3}He, and ^{4}He distributions becomes a little more complicated since the neighboring isotopes are quite abundant and have an impact on the fitting. For that reason we applied a suppression procedure to the abundant neighbor, which will be further discussed in the following section. Consequently, we applied a double Gaussian fit to the histograms (see Figures 7 (bottom) and 8), and the whole process was done in a more elaborated manner compared to the analysis presented in Adriani et al. (2013b). We went through three steps: we first did the double Gaussian fitting with all six parameters left free (mean, sigma, and peak of both isotopes) and then analyzed how the values for the means and the sigmas varied with kinetic energy. They followed a trend in kinetic energy, and in a second step we fitted appropriate functions sigma $= f(E_{\mathrm{kin}})$ and mean $= f(E_{\mathrm{kin}})$ to them. All the means and the sigmas nicely followed this trend except at the high-energy end, which may be due to the increasing contribution from the more abundant neighboring isotopes. As a consequence, we decided to perform the final fitting to the distributions by fixing the mean and the sigmas according to the function and used in the final double Gaussian fitting process only two free parameters: the two heights of the curve's peaks.

Figure 8 shows the $1/\beta$ distributions used to select ^{3}He (bottom panel) and ^{4}He (top panel) in the kinetic energy

Table 2
Hydrogen Isotope Fluxes and Their Ratio Derived with the Calorimeter; Errors Are Statistical and Systematic, Respectively

Kinetic Energy at Top of Payload (GeV n^{-1})	^{1}H Flux (GeV n^{-1} m^2 s sr)$^{-1}$	^{2}H Flux (GeV n^{-1} m^2 s sr)$^{-1}$	^{2}H/^{1}H
0.228–0.250	(1.421 ± 0.006 ± 0.055) · 10^3	(37.0 ± 0.7 ± 2.0)	(2.60 ± 0.05 ± 0.24) · 10^{-2}
0.250–0.274	(1.474 ± 0.005 ± 0.057) · 10^3	(35.8 ± 0.7 ± 1.9)	(2.43 ± 0.05 ± 0.22) · 10^{-2}
0.274–0.300	(1.504 ± 0.005 ± 0.058) · 10^3	(36.0 ± 0.6 ± 1.9)	(2.40 ± 0.04 ± 0.22) · 10^{-2}
0.300–0.329	(1.528 ± 0.005 ± 0.058) · 10^3	(36.2 ± 0.6 ± 1.9)	(2.37 ± 0.04 ± 0.22) · 10^{-2}
0.329–0.361	(1.528 ± 0.004 ± 0.058) · 10^3	(35.2 ± 0.6 ± 1.9)	(2.30 ± 0.04 ± 0.21) · 10^{-2}
0.361–0.395	(1.534 ± 0.004 ± 0.058) · 10^3	(33.1 ± 0.5 ± 1.7)	(2.16 ± 0.03 ± 0.19) · 10^{-2}
0.395–0.433	(1.513 ± 0.004 ± 0.057) · 10^3	(31.7 ± 0.5 ± 1.7)	(2.09 ± 0.03 ± 0.19) · 10^{-2}
0.433–0.475	(1.498 ± 0.003 ± 0.056) · 10^3	(30.6 ± 0.5 ± 1.6)	(2.04 ± 0.03 ± 0.18) · 10^{-2}
0.475–0.520	(1.483 ± 0.003 ± 0.056) · 10^3	(29.6 ± 0.4 ± 1.6)	(2.00 ± 0.03 ± 0.18) · 10^{-2}
0.520–0.570	(1.441 ± 0.003 ± 0.054) · 10^3	(28.2 ± 0.4 ± 1.5)	(1.96 ± 0.03 ± 0.18) · 10^{-2}
0.570–0.625	(1.386 ± 0.003 ± 0.052) · 10^3	(26.2 ± 0.4 ± 1.4)	(1.89 ± 0.03 ± 0.17) · 10^{-2}
0.625–0.685	(1.314 ± 0.002 ± 0.049) · 10^3	(24.1 ± 0.3 ± 1.3)	(1.84 ± 0.03 ± 0.17) · 10^{-2}
0.685–0.750	(1.248 ± 0.002 ± 0.047) · 10^3	(22.2 ± 0.3 ± 1.2)	(1.78 ± 0.03 ± 0.16) · 10^{-2}
0.750–0.822	(1.179 ± 0.002 ± 0.044) · 10^3	(20.3 ± 0.3 ± 1.1)	(1.73 ± 0.03 ± 0.16) · 10^{-2}
0.822–0.901	(1.097 ± 0.002 ± 0.041) · 10^3	(18.9 ± 0.3 ± 1.0)	(1.73 ± 0.03 ± 0.16) · 10^{-2}
0.901–0.988	(1.0144 ± 0.0018 ± 0.0379) · 10^3	(17.5 ± 0.3 ± 1.0)	(1.72 ± 0.03 ± 0.16) · 10^{-2}
0.988–1.082	(9.216 ± 0.016 ± 0.343) · 10^2	(15.6 ± 0.3 ± 1.1)	(1.70 ± 0.03 ± 0.18) · 10^{-2}

Table 3
Helium Isotope Fluxes and Their Ratio Derived with the ToF; Errors Are Statistical and Systematic, Respectively

Kinetic Energy at Top of Payload (GeV n^{-1})	^{4}He Flux (GeV n^{-1} m^2 s sr)$^{-1}$	^{3}He Flux (GeV n^{-1} m^2 s sr)$^{-1}$	^{3}He/^{4}He
0.126–0.141	(2.302 ± 0.019 ± 0.084) · 10^2	(18.0 ± 0.7 ± 0.7)	(7.8 ± 0.3 ± 0.6) · 10^{-2}
0.141–0.158	(2.392 ± 0.017 ± 0.085) · 10^2	(20.4 ± 0.7 ± 0.8)	(8.5 ± 0.3 ± 0.6) · 10^{-2}
0.158–0.177	(2.443 ± 0.016 ± 0.086) · 10^2	(21.9 ± 0.6 ± 0.8)	(9.0 ± 0.2 ± 0.6) · 10^{-2}
0.177–0.198	(2.501 ± 0.015 ± 0.087) · 10^2	(23.9 ± 0.5 ± 0.8)	(9.6 ± 0.2 ± 0.7) · 10^{-2}
0.198–0.222	(2.514 ± 0.013 ± 0.086) · 10^2	(25.0 ± 0.5 ± 0.9)	(10.0 ± 0.2 ± 0.7) · 10^{-2}
0.222–0.249	(2.522 ± 0.012 ± 0.086) · 10^2	(26.3 ± 0.5 ± 0.9)	(1.043 ± 0.019 ± 0.072) · 10^{-1}
0.249–0.279	(2.464 ± 0.011 ± 0.084) · 10^2	(26.7 ± 0.4 ± 0.9)	(1.082 ± 0.018 ± 0.074) · 10^{-1}
0.279–0.312	(2.413 ± 0.010 ± 0.082) · 10^2	(27.5 ± 0.4 ± 0.9)	(1.140 ± 0.017 ± 0.078) · 10^{-1}
0.312–0.350	(2.310 ± 0.009 ± 0.078) · 10^2	(27.6 ± 0.4 ± 0.9)	(1.196 ± 0.017 ± 0.081) · 10^{-1}
0.350–0.392	(2.226 ± 0.009 ± 0.075) · 10^2	(27.6 ± 0.3 ± 0.9)	(1.239 ± 0.016 ± 0.084) · 10^{-1}
0.392–0.439	(2.105 ± 0.008 ± 0.071) · 10^2	(27.1 ± 0.3 ± 0.9)	(1.289 ± 0.016 ± 0.087) · 10^{-1}
0.439–0.492	(1.922 ± 0.007 ± 0.065) · 10^2	(26.3 ± 0.3 ± 0.9)	(1.367 ± 0.016 ± 0.093) · 10^{-1}
0.492–0.551	(1.802 ± 0.006 ± 0.061) · 10^2	(25.2 ± 0.3 ± 0.9)	(1.400 ± 0.015 ± 0.096) · 10^{-1}
0.551–0.618	(1.669 ± 0.006 ± 0.056) · 10^2	(24.8 ± 0.2 ± 0.9)	(1.488 ± 0.016 ± 0.103) · 10^{-1}
0.618–0.692	(1.536 ± 0.005 ± 0.052) · 10^2	(23.7 ± 0.2 ± 0.9)	(1.543 ± 0.016 ± 0.110) · 10^{-1}
0.692–0.776	(1.383 ± 0.005 ± 0.048) · 10^2	(22.2 ± 0.2 ± 0.9)	(1.602 ± 0.016 ± 0.119) · 10^{-1}
0.776–0.870	(1.244 ± 0.004 ± 0.045) · 10^2	(19.81 ± 0.19 ± 0.87)	(1.593 ± 0.016 ± 0.127) · 10^{-1}

interval 0.439–0.492 GeV/n corresponding to 1.51–1.62 GV for ^{3}He and 2.01–2.15 GV for ^{4}He.

3.3.2. Raw Isotope Numbers with the ToF: Suppression of Abundant ^{1}H and ^{4}He

As was already discussed in Adriani et al. (2013b), the large proton background in the $Z = 1$ sample requires an additional selection in the ToF analysis to suppress the protons at higher energies (roughly 500 MeV/n). Otherwise the Gaussian fit for the protons in the $1/\beta$ distributions affects the fit for the much less abundant ^{2}H neighbor, especially at higher energies, where the mass resolution is not sufficient for a clear particle separation. To suppress the abundance of protons, we choose the energy loss measurements in the silicon layers of the tracking system and in the scintillators of the ToF versus the rigidity. The tracking system provides up to 12 energy loss measurements, while the ToF provides six. In order to further improve the separation between the isotopes, we did not take the mean of the dE/dx measurements but chose the lowest one. This minimizes the Landau fluctuations similar to the truncated mean technique, which we use in the calorimeter analysis. The two cuts were chosen in such a way that for low energies the protons could be rejected down to a very low level, by keeping practically all ^{2}H. For more details of the specific cuts, see Figure 6 in Adriani et al. (2013b).

At higher energies, the proton contamination will increase and there will be a loss of ^{2}H. This efficiency was studied with

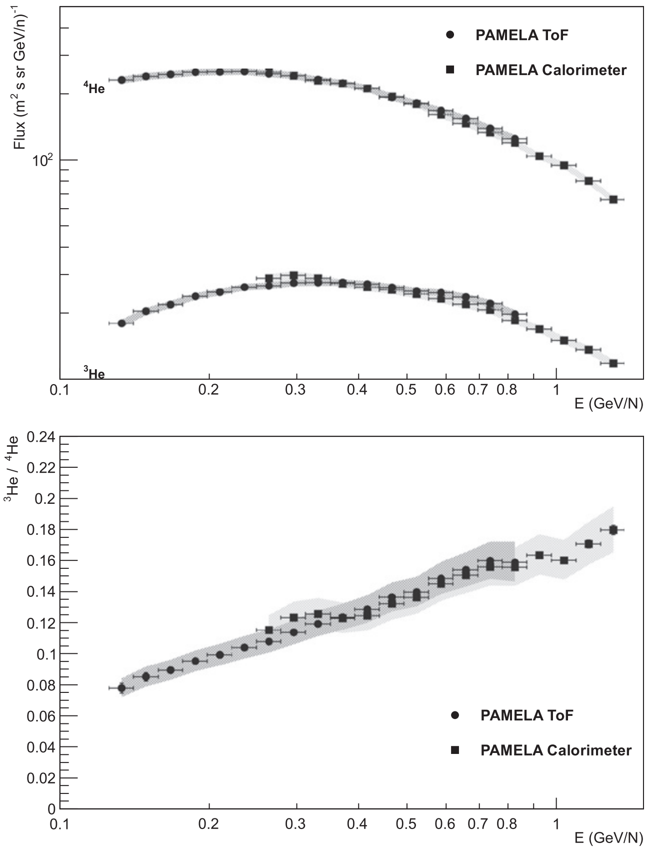

Figure 14. ^{4}He and ^{3}He absolute fluxes (top) and their ratio (bottom) derived with the ToF (circles) or the calorimeter (squares). Error bars show statistical uncertainty, and shaded areas show systematic uncertainty.

the clean ^{2}H sample provided by the calorimeter and was taken into account in the calculation of the fluxes (Section 3.4).

In the $Z = 2$ data, the level of the ^{4}He background in the ^{3}He sample is much smaller compared to the $Z = 1$ data, but similar checks like the one described above showed that also in this case a soft cut to suppress ^{4}He at higher energies improved the ^{3}He selection. We used a cut analog to the $Z = 1$ analysis based on the lowest energy release in the tracking system. Note that this suppression was not used for the $Z = 2$ analysis in Adriani et al. (2013b).

3.3.3. Raw Isotope Numbers with the Calorimeter

For the ToF system, the $1/\beta$ distributions were analyzed by fitting with Gaussians. The dE/dx distributions of the calorimeter have a non-Gaussian shape, so one has to model the expected distributions of the observable quantities and then perform likelihood fits. We used the "RooFit" toolkit (Verkerke & Kirkby 2011) for the likelihood fits. First one has to create the expected dE/dx distributions ("probability density function": PDF) for each isotope. We used the full Monte Carlo simulation of the PAMELA apparatus based on the `GEANT4` code (Agostinelli et al. 2003), which was described in Adriani et al. (2013b), for this task.

When taking the simulated energy loss in each layer as coming from `GEANT4`, we noticed that the resulting PDFs showed a slight mismatch from the flight data. We found that the width of the histograms was smaller than in the real data, and there was a small offset of about 1%–2%. We applied a multiplicative factor to the simulated energy loss in a layer and added a Gaussian spread of the signal of a few percent.

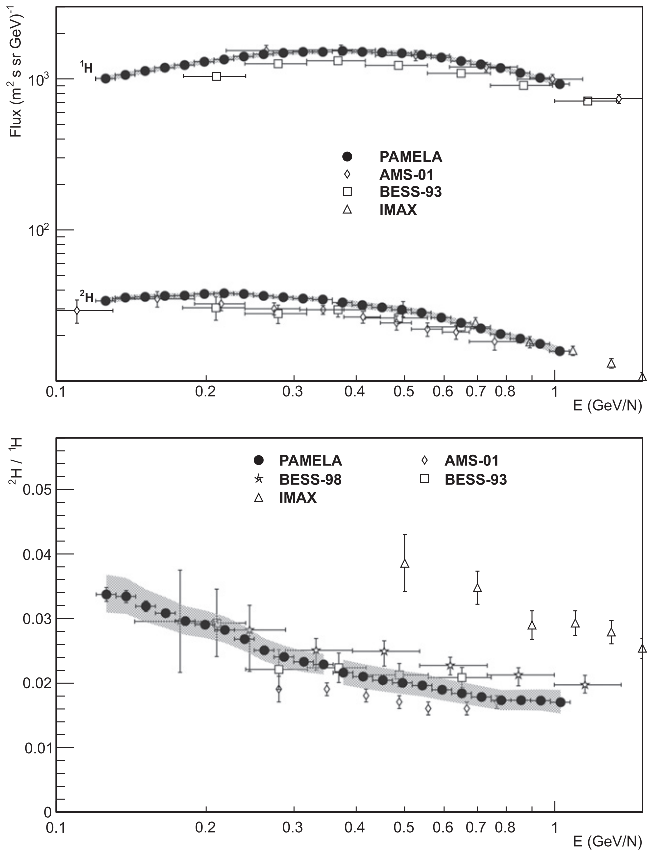

Figure 15. ^{1}H and ^{2}H absolute fluxes (top) and their ratio (bottom). For energies less than 361 MeV/n, the ToF results (Table 1) were used, and for higher energies the calorimeter results were used (Table 2). The previous experiments are AMS-01 (Lamanna et al. 2001; AMS Collaboration et al 2002; Aguilar et al. 2011), BESS-93 (Wang et al. 2002), BESS-98 (Myers et al. 2005), and IMAX (de Nolfo et al. 2000). Error bars show the statistical uncertainty, and shaded areas show the systematic uncertainty.

As an example, we show in Figure 9 the truncated mean distributions for helium in the 0.439–0.492 GeV/n kinetic energy range for ^{4}He (top) and ^{3}He (bottom). The dashed line shows how the combined fit using the two PDFs derived with the modified `GEANT4` simulation matches the data points (black points), while the solid line shows the estimated individual ^{3}He and ^{4}He signals. The kinetic energy range is the same as shown in Figure 8 for the ToF: the difference in the isotopic separation is clearly visible.

Because of the redundant detectors of PAMELA, we were able to test the simulated PDFs with real data from the instrument. Figure 2 illustrates the mass resolution that can be obtained by combining the mean dE/dx measurement in the tracker and the rigidity measurement with the magnetic spectrometer, and Figure 3 shows a similar picture using the velocity measurement from the ToF and the rigidity measurement.

By using appropriate selection cuts, we separated a proton sample and asked for the energy loss response in the calorimeter. This result was then compared to the simulated distribution. Such a comparison is shown in Figure 10 for the rigidity interval 1.80 GV–1.89 GV. (The rigidity interval in this figure is the same as in Figure 7 for the ToF, and here the difference in the isotopic separation is clearly visible.)

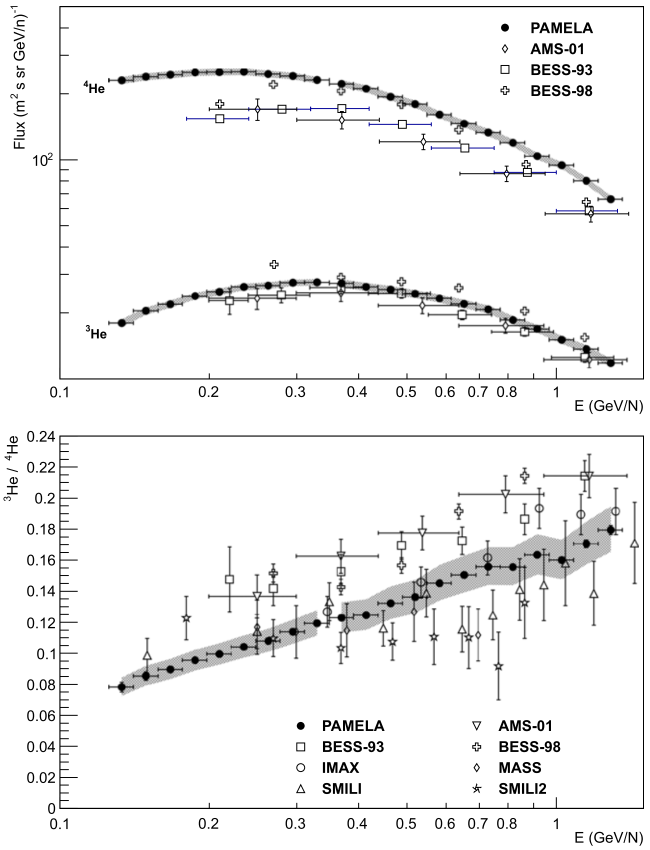

Figure 16. ^{4}He and ^{3}He absolute fluxes (top) and their ratio (bottom). For energies less than 350 MeV/n, the ToF results (Table 3) were used, and for higher energies the calorimeter results were used (Table 4). The previous experiments are AMS (Aguilar et al. 2011), BESS-93 (Wang et al. 2002), BESS-98 (Myers et al. 2003), IMAX (Reimer et al. 1998), SMILI-2 (Wefel et al. 1995), MASS (Webber et al. 1991), and SMILI-1 (Beatty et al. 1993). Error bars show statistical uncertainty, and shaded areas show systematic uncertainty.

It can clearly be seen that the flight data proton PDF shows a larger tail into the ^{2}H histogram compared to the simulated PDF. This tail will cause derivation of a lower number of ^{2}H counts compared to the simulated PDF (the difference in the ^{2}H counts is about 8% in this example).

While the creation of PDFs from flight data for ^{2}H, ^{3}He, and ^{4}He is restricted to lower energies, due to the limited isotopic separation, we created PDFs for protons up to 4 GV using strict selection cuts. In principle, a clear separation between ^{1}H and ^{2}H is not possible at these rigidities, but since the ^{1}H are so dominant, the contamination of ^{2}H in the ^{1}H sample should be very small. We observed that the tail in Figure 10 is only visible for medium energies, whereas our selection cuts for the truncated mean are quite soft. Since a small number of layers are used to derive the truncated mean, fluctuations are probably still significant, and it seems that the `GEANT4` simulation cannot fully reproduce the actual energy loss under these circumstances.

At higher energies, where our selection cuts for the calorimeter are stricter, the tails in the flight data PDF disappeared, resulting in a good agreement with the simulated PDF again. We decided to take simulated PDFs (except for the ^{1}H model) for the "RooFit" analysis in this paper.

One could argue that also for the other isotopes it might be that the simulated PDFs do not show the correct shape, missing the tail that is visible for ^{1}H, so for example we might underestimate the number of ^{3}He that contribute to the ^{4}He distribution. However, we found that the maximum difference in the ^{2}H counts at medium energies was at most 10%, with the number of ^{1}H exceeding the number of ^{2}H in the distribution by a factor of 50–100. In comparison, the $^3\text{He}/^4\text{He}$ ratio is around 0.2, so one can expect that the effect of missing tails in the simulated PDFs will have a negligible influence on the ^{3}He and ^{4}He counts.

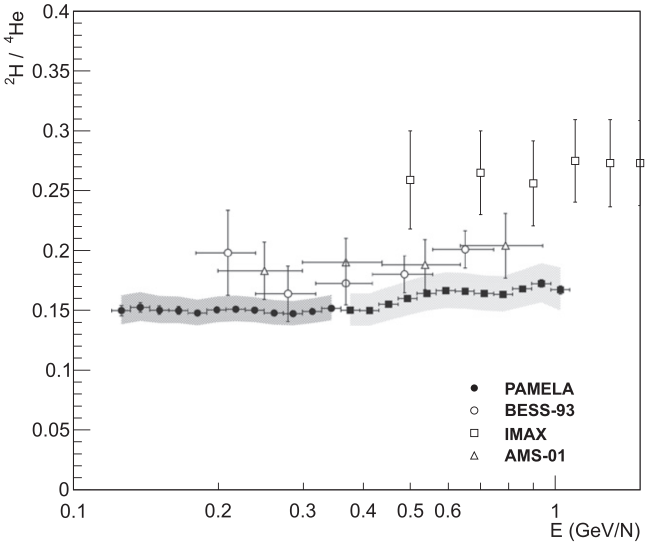

Figure 17. $^2\text{H}/^4\text{He}$ ratio compared to previous experiments: AMS-01 (Aguilar et al. 2011), BESS (Wang et al. 2002), and IMAX (de Nolfo et al. 2000). Error bars show statistical uncertainty, and shaded areas show systematic uncertainty.

3.4. *Flux Determination*

To derive the isotope fluxes, the number of ^{1}H and ^{2}H events in the $Z = 1$ sample and the number of ^{3}He and ^{4}He events in the $Z = 2$ sample had to be corrected for the selection efficiencies, particle losses, contamination, and energy losses. Most of the corrections could be taken directly from Adriani et al. (2013b), and only some efficiencies in the ToF analysis were changed, for example the efficiency for the suppression of the abundant ^{1}H and ^{4}He (see Section 3.3.2). A new correction is the efficiency for the calorimeter, which is shown in Figure 11 for specific selection cuts. The selection cuts for the actual analysis were described in Section 3.2.2. One can nicely see that this approach gives a quite high efficiency showing a rather constant behavior down to about 200 MeV/n, where the efficiency then shows a steep decrease. As mentioned already above, one can do these selections within the calorimeter analysis in various ways, but the efficiencies are very sensitive to the applied cuts. This is illustrated in Figure 11 for two other cut conditions: a strict cut where the particle has to fully traverse the calorimeter and produce a signal in the last layer, and a more relaxed cut (30 hit silicon strips). As one can see, the efficiencies of these cuts are quite low and show a steep drop already at 300–400 MeV/n. Preliminary results for the relaxed cut were presented in earlier publications (Menn et al. 2013a, 2013b).

The comparison between efficiencies derived with simulated data and the ones derived with flight data (using ToF and tracker dE/dx for selection) is shown for $Z = 2$ particles in Figure 12.

Table 4

Helium Isotope Fluxes and Their Ratio Derived with the Calorimeter; Errors Are Statistical and Systematic, Respectively

Kinetic Energy at Top of Payload (GeV n^{-1})	^{4}He Flux (GeV n^{-1} m^2 s sr)$^{-1}$	^{3}He Flux (GeV n^{-1} m^2 s sr)$^{-1}$	^{3}He/^{4}He
0.249–0.279	$(2.501 \pm 0.014 \pm 0.094) \cdot 10^2$	$(28.9 \pm 0.6 \pm 1.2)$	$(1.15 \pm 0.02 \pm 0.09) \cdot 10^{-1}$
0.279–0.312	$(2.411 \pm 0.013 \pm 0.091) \cdot 10^2$	$(29.8 \pm 0.6 \pm 1.2)$	$(1.24 \pm 0.02 \pm 0.10) \cdot 10^{-1}$
0.312–0.350	$(2.292 \pm 0.012 \pm 0.086) \cdot 10^2$	$(28.8 \pm 0.5 \pm 1.2)$	$(1.26 \pm 0.02 \pm 0.10) \cdot 10^{-1}$
0.350–0.392	$(2.222 \pm 0.011 \pm 0.083) \cdot 10^2$	$(27.4 \pm 0.5 \pm 1.1)$	$(1.23 \pm 0.02 \pm 0.10) \cdot 10^{-1}$
0.392–0.439	$(2.110 \pm 0.010 \pm 0.079) \cdot 10^2$	$(26.3 \pm 0.4 \pm 1.1)$	$(1.25 \pm 0.02 \pm 0.10) \cdot 10^{-1}$
0.439–0.492	$(1.931 \pm 0.009 \pm 0.072) \cdot 10^2$	$(25.6 \pm 0.4 \pm 1.1)$	$(1.32 \pm 0.02 \pm 0.10) \cdot 10^{-1}$
0.492–0.551	$(1.791 \pm 0.008 \pm 0.067) \cdot 10^2$	$(24.4 \pm 0.3 \pm 1.0)$	$(1.36 \pm 0.02 \pm 0.11) \cdot 10^{-1}$
0.551–0.618	$(1.601 \pm 0.007 \pm 0.059) \cdot 10^2$	$(23.3 \pm 0.3 \pm 1.0)$	$(1.45 \pm 0.02 \pm 0.11) \cdot 10^{-1}$
0.618–0.692	$(1.455 \pm 0.007 \pm 0.054) \cdot 10^2$	$(22.0 \pm 0.3 \pm 0.9)$	$(1.51 \pm 0.02 \pm 0.12) \cdot 10^{-1}$
0.692–0.776	$(1.327 \pm 0.006 \pm 0.049) \cdot 10^2$	$(20.7 \pm 0.3 \pm 0.9)$	$(1.56 \pm 0.02 \pm 0.12) \cdot 10^{-1}$
0.776–0.870	$(1.190 \pm 0.006 \pm 0.044) \cdot 10^2$	$(18.6 \pm 0.2 \pm 0.8)$	$(1.56 \pm 0.02 \pm 0.12) \cdot 10^{-1}$
0.870–0.974	$(1.034 \pm 0.005 \pm 0.038) \cdot 10^2$	$(16.9 \pm 0.2 \pm 0.7)$	$(1.64 \pm 0.02 \pm 0.13) \cdot 10^{-1}$
0.974–1.092	$(93.8 \pm 0.5 \pm 3.5)$	$(15.1 \pm 0.2 \pm 0.6)$	$(1.60 \pm 0.02 \pm 0.13) \cdot 10^{-1}$
1.092–1.223	$(79.7 \pm 0.4 \pm 3.0)$	$(13.63 \pm 0.20 \pm 0.59)$	$(1.71 \pm 0.03 \pm 0.14) \cdot 10^{-1}$
1.223–1.371	$(65.5 \pm 0.4 \pm 2.4)$	$(11.80 \pm 0.18 \pm 0.52)$	$(1.80 \pm 0.03 \pm 0.15) \cdot 10^{-1}$

As one can see, there is a good agreement at low energies for ^{3}He and some difference at higher energies, whereas it is the opposite for ^{4}He. We decided to use the flight data efficiencies at lower energies and then for higher energies (roughly around 700 MeV/n in Figure 12) follow the trend of the simulated efficiencies by applying a constant correction factor. The same method was used for ^{2}H efficiency, while for ^{1}H we used the flight data efficiency for the full energy range.

The following corrections are taken from Adriani et al. (2013b) without changes, and we refer to this paper for more details:

1. Due to hadronic interactions in the aluminum pressurized container (2 mm thick) and the top scintillators, helium and hydrogen nuclei might be lost. The correction factor $b(E)$ is different for each isotope and has been derived from the Monte Carlo simulation, being $\simeq$6% for ^{1}H, $\simeq$10% for ^{2}H, and $\simeq$13% for both helium isotopes,.
2. The nominal geometrical factor G_F of PAMELA is almost constant above 1 GV, with the requirements on the fiducial volume corresponding to a value of $G_F = 19.9$ cm^2 sr; for lower energies the bending of the particle track leads to a decrease. The nominal geometrical factor G_F was multiplied with the correction factor $b(E)$ to get an effective geometrical factor $G(E)$; see Figure 7 in Adriani et al. (2013b).
3. Regarding the contribution to ^{2}H from inelastic scattering of ^{4}He, this background was derived from the simulation and subtracted from the raw ^{2}H counts. The contamination is on the order of $\simeq$10% at 100 MeV/n, going down with increasing energy ($\simeq$1% at 600 MeV/n); see Figure 8 in Adriani et al. (2013b). The contamination in the ^{3}He sample from ^{4}He fragmentation was also evaluated and was found to be very small (less than 1%). This was included in the systematic uncertainty of the measurement.
4. The measured particle spectra are distorted due to particle slowdown (caused by the energy loss) and the finite resolution of the spectrometer. We used a Bayesian unfolding procedure (D'Agostini 1995) to derive the number of events at the top of the payload (see Adriani et al. 2011).

The differential flux is then given by

$$\Phi_{\mathrm{ToP}}(E) = \frac{N_{\mathrm{ToP}}(E)}{TG(E)\Delta E}, \tag{4}$$

where $N_{\mathrm{ToP}}(E)$ is the unfolded particle count (corrected for the selection efficiencies) for energy E, ΔE is the energy bin width, and $G(E)$ is the effective geometrical factor as described above. The live time, T, depends on the orbital selection as described in Section 3.1 and is evaluated by the trigger system (Bruno 2008).

3.5. Systematic Uncertainties

The systematic uncertainties presented in Adriani et al. (2013b) have been reviewed and updated to the new analysis methods when necessary.

The event selection criteria described in Section 3.1 were similar to previous work on high-energy proton and helium fluxes; see Adriani et al. (2011). In that paper the systematic errors of the selection have been studied using flight data and simulations, resulting in a quoted systematic uncertainty of about 4%. This error is used also in this work.

As already described in Section 3.3.2, the quality of the Gaussian fit procedure in the ToF analysis was tested using the truncated mean of the energy deposited in the electromagnetic calorimeter to select pure samples of ^{1}H, ^{2}H, ^{3}He, and ^{4}He from noninteracting events. For the abundant particles ^{1}H and ^{4}He, the number of reconstructed events from the Gaussian fit was found to agree with the number of events selected with the calorimeter practically over the full energy range, while for ^{2}H and ^{3}He there were some systematic differences of some percent in the highest energy bins. Note that without the additional cuts that reject the more abundant ^{1}H and ^{4}He, the differences would be much larger. We assigned a systematic uncertainty of 0.5% for low and medium energies, increasing to 4% at 600 MeV/n for ^{2}H and to 3% at 800 MeV/n for ^{3}He. For ^{1}H the systematic uncertainty was set constant to 0.5%, while for ^{4}He it was set to be energy dependent, increasing to 1.5% at 800 MeV/n.

A similar systematic error is assigned to the fit procedure made with the calorimeter. Here deviations between the model PDF and the flight data will transform into a systematic difference in the number of reconstructed events. However, we have no other detector to select pure samples of the isotopes. Therefore, we studied how a misplacement of the model PDFs transferred to different particle counts. Similar to the results for the ToF, it was found that the effect on the number of reconstructed events was much more pronounced for ^{2}H and ^{3}He compared to ^{1}H and ^{4}He and that the effect increased with energy. However, the misplacement of the model PDFs can be checked by using the abundant ^{1}H and ^{4}He as a reference (for example, comparing the peaks in the distributions), thus limiting the systematic differences in the number of reconstructed events to some percent in the highest energy bins. Similar to the systematic error for the ToF, we assigned a systematic uncertainty of 0.5% for low and medium energies, increasing to 4% at 1000 MeV/n for ^{2}H and to 3% at 1400 MeV/n for ^{3}He. The ^{1}H systematic uncertainty was set constant to 0.5%, while for ^{4}He it was set again to be energy dependent, increasing to 1.5% at 1400 MeV/n.

The efficiency of the calorimeter selection was derived using simulated and flight data, as shown for $Z = 2$ particles in Figure 12. For $Z = 2$ data the agreement between the two methods is quite good, and we assigned a conservative systematic error of 2% for ^{4}He and 3% for ^{3}He independent from the energy. For $Z = 1$ particles, the difference between the two methods is larger. As stated above, for ^{1}H we used the flight data efficiency for the full energy range, which should result in a small systematic error since the ^{1}H are so abundant and therefore the contamination of other particles is negligible. We assigned a conservative systematic error of 2%. For the ^{2}H efficiency, we used the flight data efficiencies at lower energies but followed the trend of the simulated efficiencies by applying a constant correction factor for higher energies; we estimated a systematic error of 5%.

The following systematic uncertainties are taken from Adriani et al. (2013b) without changes, and we refer to this paper for more details:

1. The systematic uncertainty on the ^{2}H flux resulting from the subtraction of secondary ^{2}H from ^{4}He spallation is 1.9% at low energy, dropping below 0.1% at 300 MeV/n because of the finite size of the Monte Carlo sample. The validity of the Monte Carlo simulation has been tested in Adriani et al. (2013b) using the ^{3}H component in the flight data sample; see Figure 7.
2. The systematic uncertainty on the unfolding procedure has been discussed in Adriani et al. (2011) and was found to be 2%, independent of energy.
3. The selection of galactic particles was described in Section 3.1, and the correction for particles lost because of this selection has an uncertainty that is due to the size of the Monte Carlo sample. The systematic error decreases from 6% at 120 MeV/n to 0.06% at 1000 MeV/n.
4. The uncertainty on the effective geometrical factor as estimated from the Monte Carlo simulation is 0.18%, practically independent of energy.

The systematic uncertainties are included in Tables 1–4 and in Figures 13–17.

4. RESULTS AND DISCUSSION

In Figures 13 and 14 we show the hydrogen and helium isotope fluxes (top) and the ratios of the fluxes (bottom) measured with the ToF or the calorimeter. The results are also reported in Tables 1–4.

It is worth noting that the PAMELA results obtained via the ToF analysis and via the multiple dE/dx measurements with the calorimeter agree very well within their systematic errors. This gives confidence in the results.

In direct comparison with our first paper (Adriani et al. 2013b), the results obtained via the ToF analysis in this work show some differences from our earlier results. While the ^{1}H fluxes show only minor differences, the ^{2}H flux is roughly 5% higher in this work. The ^{4}He flux is almost 10% higher at the lowest energy bin, at the highest energies the new ^{4}He flux is about 10% lower, and at medium energies around 400 MeV/n the two results agree. The new ^{3}He flux is about 3%–4% lower for most of the energy range; for energies above 500 MeV/n the difference increases and reaches about 15% for the highest energy bins. We attribute this to the changes in the fitting procedure (for example, the double Gaussian fit for ^{4}He and the fixing of parameters) and improvements in the efficiency calculation compared to the first paper. Based on this more comprehensive analysis presented here, these results supersede the previous ones.

To compare our isotope fluxes with other measurements, we decided to use at low energies only the ToF results (up to 361 MeV/n for hydrogen and up to 350 MeV/n for helium) and above these values only use the calorimeter results. In Figures 15 and 16 we show these hydrogen and helium isotope fluxes (top) and the ratios of the fluxes (bottom), compared to previous measurements (Webber et al. 1991; Beatty et al. 1993; Wefel et al. 1995; Reimer et al. 1998; de Nolfo et al. 2000; Lamanna et al. 2001; Myers et al. 2003, 2005; AMS Collaboration et al 2002; Wang et al. 2002; Aguilar et al. 2011).

Figure 17 shows the ^{2}H/^{4}He ratio as a function of kinetic energy per nucleon.

It is visible that the former results show a large spread, and it is obvious that the PAMELA results are more precise in terms of statistics. In this context it is important to know that all the former measurements shown in Figures 15–17, except AMS-01, are from balloon-borne experiments and thus are affected by the nonnegligible background of atmospheric secondary particle production.

The scientific interest in these isotopes of ^{1}H, ^{2}H, ^{3}He, and ^{4}He is determined by the question about their origin. It is believed that the protons and the ^{4}He particles are predominantly of primary origin and thus arise directly from their sources, whereas ^{2}H and ^{3}He are of secondary origin and thus are produced by interactions of these primaries with the interstellar gas. The interpretation of these results then allows us to study more in detail the conditions of their propagation in the interstellar space. Beside these light isotopes presented here, there are more particles of secondary origin that are used in these studies, such as sub-iron particles or lithium, beryllium, and boron. The effort aims to develop a diffusion model that will describe the propagation of charged particles and their lifetime in our Galaxy. This will also help us to better understand the energy density of different components within interstellar space, such as magnetic fields, electromagnetic radiation, gas pressure, and cosmic rays. These model calculations have to deal with a number of parameters, which have their origin in astrophysics, in nuclear physics, and in high-energy particle physics. The advantage of the light isotopes ^{2}H and ^{3}He in this context compared to the more heavy secondary particles lies in the fact that they do not have so many progenitors compared to the sub-iron particles or to lithium, beryllium, and boron: it is predominantly ^{4}He. A comprehensive and detailed study and discussion and interpretation of our results in this context is beyond the scope of this paper, but we like to refer to a recent paper published by Coste et al. (2012).

We acknowledge support from the Russian Space Agency (Roscosmos), the Russian Foundation for Basic Research (grant 13-02-00298), the Russian Scientific Foundation (grant 14-12-00373), the Italian Space Agency (ASI), Deutsches Zentrum fur Luft- und Raumfahrt (DLR), the Swedish National Space Board, and the Swedish Research Council.

REFERENCES

Adriani, O., Barbarino, G. C., Bazilevskaya, G. A., et al. 2011, Sci, 332, 69
Adriani, O., Barbarino, G. C., Bazilevskaya, G. A., et al. 2013a, ApJ, 765, 91
Adriani, O., Barbarino, G. C., Bazilevskaya, G. A., et al. 2013b, ApJ, 770, 2
Agostinelli, S., Allison, J., Amako, K., et al. 2003, NIMPA, 506, 250
Aguilar, M., Alcaraz, J., Allaby, J., et al. 2011, ApJ, 736, 105
AMS Collaboration, Aguilar, M., Alcaraz, J., et al. 2002, PhR, 366, 331
Beatty, J. J., Ficenec, D. J., Tobias, S., et al. 1993, ApJ, 413, 268
Boezio, M., Bonvicini, V., Mocchiutti, E., et al. 2002, NIMPA, 487, 407
Bonechi, L., Adriani, O., Bongi, M., et al. 2006, NIMPA, 570, 281
Brun, R., & Rademakers, F. 1997, NIMPA, 389, 81
Bruno, A. 2008, PhD thesis, Univ. Bari
Coste, B., Derome, L., Maurin, D., & Putze, A. 2012, A&A, 539, A88
D'Agostini, G. 1995, NucIM, A362, 487
de Nolfo, G. A., Barbier, L. M., Christian, E. R., et al. 2000, in AIP Conf. Proc. 528 Accelaration and Transport of Energetic Particles Observed in the Heliosphere, ed. R. A. Mewaldt et al. (Melville, NY: AIP), 425
Garcia-Munoz, M., Mason, G. M., & Simpson, J. A. 1975a, in The 14th Int. Cosmic Ray Conf. 1, 319
Garcia-Munoz, M., Mason, G. M., & Simpson, J. A. 1975b, ApJ, 202, 265
Gleeson, L. J., & Axford, W. I. 1968, ApJ, 154, 1011
Heinbach, U., & Simon, M. 1995, ApJ, 441, 209
Lamanna, G., Alpat, B., Battiston, R., et al. 2001, in The 27th Int. Cosmic Ray Conf., 1614
Leech, H. W., & O'Gallagher, J. J. 1978, ApJ, 221, 1110
MacMillan, S., & Maus, S. 2005, EP&S, 57, 1135
Menn, W., Bogomolov, E. A., Formato, V., et al. 2013b, in The 33rd Int. Cosmic Ray Conf. 0233; http://www.cbpf.br/~icrc2013/papers/icrc2013-0233.pdf
Menn, W., Bogomolov, E. A., Krut'kov, S. Y., et al. 2013a, JPhCS, 409, 012030
Mewaldt, R. A., Stone, E. C., & Vogt, R. E. 1976, ApJ, 206, 616
Myers, Z. D., Seo, E. S., Abe, K., et al. 2003, in The 28th Int. Cosmic Ray Conf., 1805
Myers, Z. D., Seo, E. S., Wang, J. Z., et al. 2005, AdSpR, 35, 151
Picozza, P., Galper, A. M., Castellini, G., et al. 2007, APh, 27, 296
Reimer, O., Menn, W., Hof, M., et al. 1998, ApJ, 496, 490
Shea, M. A., Smart, D. F., & Gentile, L. C. 1987, PEPI, 48, 200
Stephens, S. A. 1989, AdSpR, 9, 145
Strong, A. W., & Moskalenko, I. V. 1998, ApJ, 509, 212
Strong, A. W., Moskalenko, I. V., & Ptuskin, V. S. 2007, ARNPS, 57, 285
Tomassetti, N. 2012, Ap&SS, 342, 131
Verkerke, W., & Kirkby, D. 2011, arXiv:physics/0306116
Wang, J. Z., Seo, E. S., Anraku, K., et al. 2002, ApJ, 564, 244
Webber, W. R., Golden, R. L., Stochaj, S. J., et al. 1991, ApJ, 380, 230
Wefel, J. P., Ahlen, S. P., Beatty, J. J., et al. 1995, in The 24th Int. Cosmic Ray Conf. 2, 630